Composites Part B 265 (2023) 110913

Contents lists available at ScienceDirect

Composites Part B

journal homepage: www.elsevier.com/locate/compositesb

Imbibition and rheology of polymer-matrix nanoporous metal composites: Towards extrusion-based 3D printing

Amm G. Hasib [a], Stanislau Niauzorau [a], Natalya Kublik [a], Sayli Jambhulkar [a], Yizhen Zhu [b], Dharneedar Ravichandran [a], Xiangjia Li [b], Kenan Song [a,**], Bruno Azeredo [a,*]

[a] The School for Manufacturing Systems and Networks, Ira A. Fulton Schools of Engineering, Arizona State University, Mesa, AZ, 85281, USA
[b] The School for Engineering of Matter, Transport and Energy, Ira A. Fulton Schools of Engineering, Arizona State University, Tempe, AZ, 85287, USA

ARTICLE INFO

Handling Editor: Dr Hao Wang

ABSTRACT

When combined with additive manufacturing, nanoporous metals can be shaped into multifunctional and interdigitated 3D circuits with hierarchical diffusional pathways, critical for optimizing electrochemical storage devices. In an attempt to develop a method for extrusion-based additive manufacturing of nanoporous metals and their composites, this paper examines a new polymer matrix composite reinforced with spherical nanoporous copper powders (PMC-NP-Cu) synthesized by dealloying at high fill fractions (>45 vol%), that can be integrated with fused filament fabrication (FFF). The role of capillary imbibition of the polymer into the metal's nanopores was investigated by examining their wettability, rheology, and density as a function of polymer's molecular weight (MW) particularly for a range of radius of gyration (R_g) between 2 and 20 nm comparable to its average pore size (22 nm). It was found that the melt viscosity of PMC-NP-Cu with the shortest M_w departed from classical viscosity scaling (i.e., $\eta \infty M_W^1$) which is attributed to the polymer imbibition into nanopores and composite densification. For molecular weights equal to 5 and 200 kg/mol, it was found that the volume fraction of the reinforcing phase was 16% and 8% higher respectively when imbibition was accounted for, resulting in an increase of two orders of magnitude in its zero-shear viscosity. These results correlated to the extrudability tests of PMC-NP-Cu filaments at higher packing factors (i.e., 47 vol%) for FFF. The insight of this study might be beneficial to integrate nanoporous metals into binder-based 3D printing technology to fabricate interdigitated battery electrodes and multifunctional 3D printed electronics.

1. Introduction

Interest in high surface area nanoporous metals and their integration with freeform fabrication schemes enables fabrication of complex 2.5D and 3D designs of hierarchical structures from centimeters to nanometers scale, with each length scale synergistically serving unique functionalities. Particularly, nanoporous metals that exhibit bi-continuous pore and solid networks [1] have unique inherent properties such as high specific surface area [2], higher chemical reactivity [3] and enhanced ionic, phononic and electronic transport properties [4–6]. Advanced manufacturing methods such as microfabrication [7], directed- or self-assembly and templating methods [8,9], or 3D printing have trade-offs in resolution, design flexibility and throughput to build hierarchical architectures at micro-, mm- and cm-scale into functional devices. For example, (a) two-photon 3D nanolithography was used to template nanoscale architected metal foams which deterministically defined open-architected porosity with the finest sub-100 nm resolution [10], and (b) multiple lithographical steps and self-assembly were used to template interdigitated nickel inverse-opal porous electrodes for batteries [11].

Recently, the route of chemical dealloying 3D printed solid precursor alloys was explored and yielded nanoporous gold [12] and copper 3D structures [13] with macroscopic and hierarchical dimensions supported by the resolution of selective laser melting (SLM) (i.e., ~100–300 μm). Dealloying is an electrolytic or electroless etching process in which the less noble element of a precursor alloy is selectively etched by an acidic or alkaline media resulting in adatom formation and clustering yielding a nanoporous structure [14–16]. However, dealloying of 3D printed precursors has drawbacks such as (i) the inherent shrinkage and internal residual stress associated with dealloying that are

* Corresponding author.
** Corresponding author.
E-mail addresses: kenan.song@asu.edu (K. Song), bruno.azeredo@asu.edu (B. Azeredo).

https://doi.org/10.1016/j.compositesb.2023.110913
Received 16 March 2023; Received in revised form 21 June 2023; Accepted 27 July 2023
Available online 8 August 2023

Table 1
Polymer grades and their physical properties.

Product Grade	Theoretical M_w, g/mol	Degree of polymerization, X_n $\left(\frac{Mw\ of\ Polymer}{Mw\ of\ repeat\ unit}\right)$	Calculated bond length of monomer l, nm	Polymer chain displacement length r, nm	Polymer chain radius of gyration, R_g, nm
Aquazol 5	5k	50.5	0.454	5	2
Aquazol 50	50k	505.1		10	6
Aquazol 200	200k	2020.2		20	12
Aquazol 500	500k	5050.5		35	19

imposed on 3D printed parts resulting in shape distortion and dimensional inaccuracies, and (ii) the complex process-structure relationships associated with rapid solidification of laser based methods (i.e., SLM) which regulates the final phase of the printed precursor and, thus, alters the pore morphology after its dealloying step in post-processing [17].

Contrary to that, extrusion-based metal additive manufacturing techniques such as Fused Filament Fabrication (FFF) offers a low-cost route to manufacture 3D printed prototypes and combining this technology with dealloying can pave the way to produce high surface area conductive circuitries keeping the original microstructure unaltered. However, this process route has not been explored much due to roadblocks such as: (i) lack of a flowable composites reinforced with nanoporous powders that can support moderate viscosities at high shear rates (10-100s^{-1}) and at high fill fractions (>50 vol%) [18], and (ii) lack of understanding of capillary-driven polymer imbibition into the nanoporous powders when they are solution mixed, as it alters the powder fill-fraction and composite melt rheology which limits its extrudability and printability. If not resolved, these problems lead to low green-part density which leads to excessive shrinkage during debinding and sintering and, overall, contributes to poor mechanical performance [19,20].

Understanding capillary-driven imbibition into nanopores becomes critical to manufacturing processes. In fact, imbibition is a key phenomenon in flexographic printing [21,22], inkjet printing [23,24], petroleum oil recovery [25,26], and nanofluidic transport [27,28]. In the extrusion and FFF printing of PMC-NP-Cu, there is a need to know the volume fraction of the powders in the composite since that needs to be maximized to minimize shrinkage [18] and, at the same time, to support laminar flow at high-shear rates to provide good adhesion to the walls of the extruder [18]. Since the degree of imbibition of polymeric solution into dealloyed nanoporous metals had never been studied as a function of molecular weight particularly for a radius of gyration that is compared to the pore size of the metal host, it was an interesting area to explore in this study.

In this paper, it was sought to combine chemical dealloying with extrusion-based metal additive manufacturing technique to produce 3D high surface area solids (dealloyed from known precursor phases) without residual stresses. This was accomplished by dealloying gas-atomized precursor Cu–Al powders prior to 3D printing to obtain spherical and flowable nanoporous copper (NP–Cu) that can be readily mixed into a polymer-matrix composite (PMC-NP-Cu) forming a feedstock for extrusion. On a more fundamental note, this paper sought to quantify (i) the wetting and imbibition of polymer solutions and melts into the nanopores as function of polymer M_w and (ii) the resulting

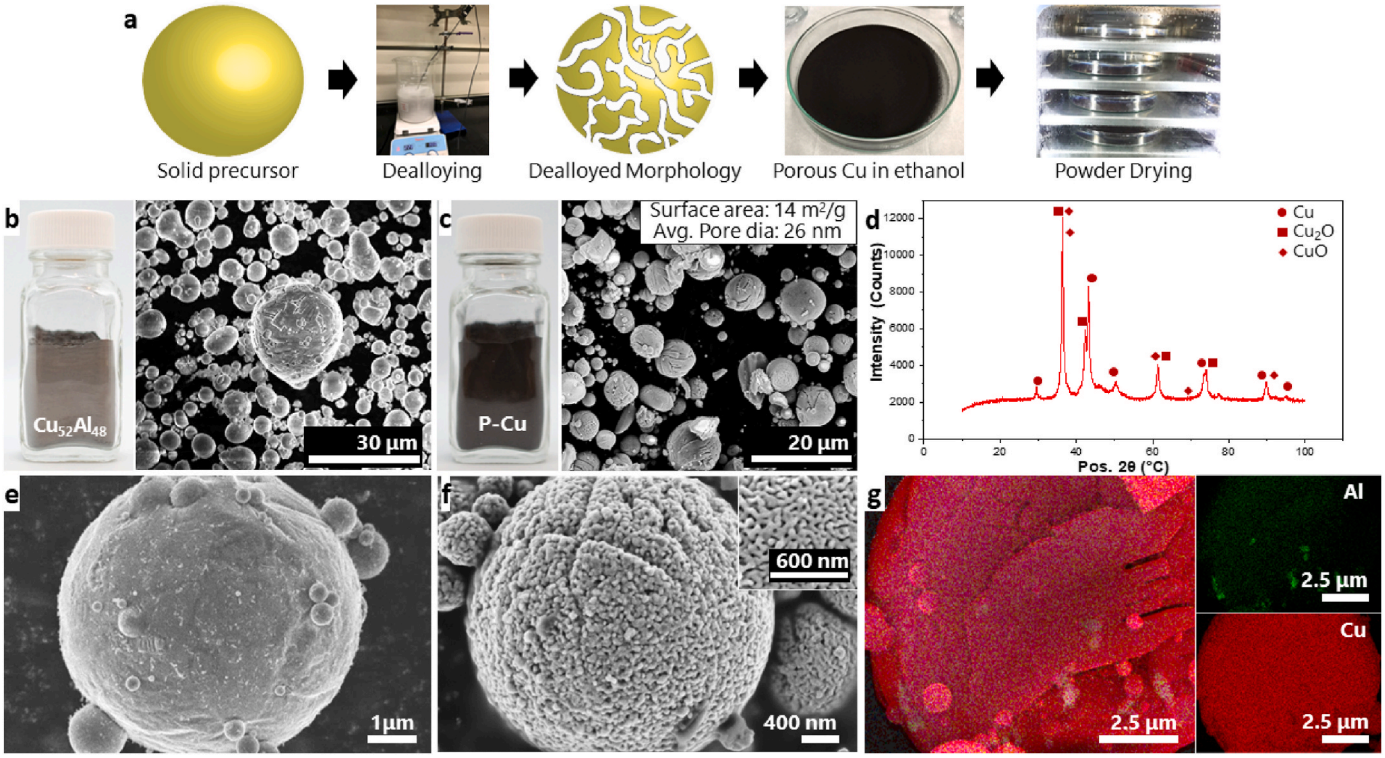

Fig. 1. (a) The step-by-step preparation of dried dealloyed nanoporous Cu (NP–Cu), (b) SEM image of the precursor CuAl powders,(c) dealloyed NP-Cu powders, (d) XRD spectra of NP-Cu powders with an oxide passivation layer showing different peaks, (e) higher magnification image of a single CuAl powder, (f) single NP-Cu powder and (g) EDS mapping of a single NP-Cu powder demonstrating minimal residual Al after dealloying.

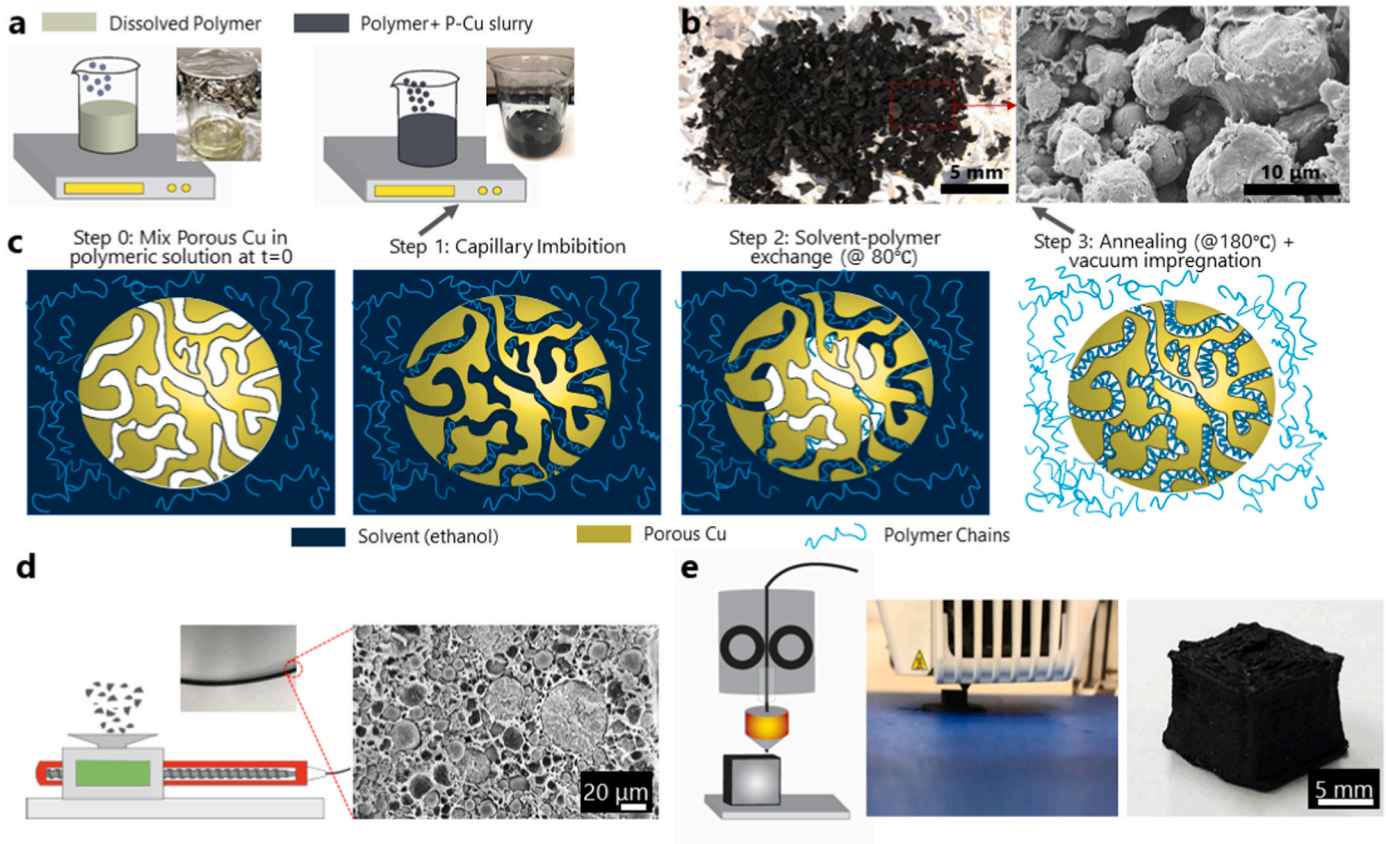

Fig. 2. (a) Solution mixing of porous metal powders with dissolved polymers to obtain the composite suspension, (b) feedstock made from the dried and solidified composite suspension by mechanical cleaving, (c) step-by-step process of polymer imbibition into host metal powder nanopores during mixing with dissolved Aquazol (step 1) and NP-Cu, solvent-polymer exchange under vacuum at 80 °C (step 2) and high temperature annealing under vacuum (step 3), (d) extruded filament made out of 50 vol% NP-Cu and cross-sectional SEM image of one of its facets, and (e) 3D printing of PMC-NP-Cu-Aquazol and a 3D printed part consisting 40 vol% packing of NP-Cu by design and 47 vol% when considering imbibition.

effects on the composite's skeletal density and in the melt rheological characteristics of the extruded PMC-NP-Cu filaments. It was found that, if unaccounted for, they can explain extrusion failure by observing how high degree of polymer imbibition can shift the jamming onset by increasing the actual metal powder packing fraction. Although it seems counter-intuitive to choose a high M_w thermoplastic to make the PMC-NP-metal composite to achieve successful extrusion, it was found that it was the preferred composite to design a successful binder based additive manufacturing solution. This paper is a step toward developing an extrudable feedstock for facile, low cost FFF printing of high surface area circuitries, battery electrodes and concomitant 3D printing of highly conductive metal and non-conductive polymer.

2. Experimental section

2.1. Materials

Four different sets of Aquazol (poly 2-ethyl-2-oxazoline) pellets (pulverized and procured from the vendor "Polymer Chemistry Innovation, Inc.") were purchased (Fig. S8) with (i) Mw values of 5k, 50k, 200k, and 500k g/mol, (ii) density of 1.14 g/cm^3 and (iii) average pellet size of 3 mm. Aquazol is an amorphous, water-soluble, non-toxic, and biodegradable polymer that was used to perform all tests conducted in this study. Polymer chain end-to-end displacement length and polymer chain radius of gyration (R_g) was calculated following the Flori-Huggins theories [29–31] (Table 1). Note that the R_g calculation is a rough estimate which does not involve the functional groups of the side chain. The following equations were used to calculate displacement length, r, and polymer chain radius of gyration, R_g:

$$\overline{r^2} = nl^2 \tag{1}$$

$$R_g = l\sqrt{\frac{N_p}{6}} \tag{2}$$

Where n is the degree of polymerization or number of monomers in the polymer, l is the calculated bond length from the polymer molecular structure and N_p is the number of bonds in the polymer structure. Gas atomized CuAl powders composed of 52.42 at.% of Cu, 47.45 at.% of Al, and 0.13 at% of Fe and Si impurities were purchased from "Powder Alloy Corporation (PAC)" to be used as our precursor alloy to produce nanoporous Cu powders. The calculated density of the precursor from its weight ratio was found to be 4.27 g/cm^3 with a mean particle size of 11.76 μm (Fig. 1 and Section A from the supplementary section to find the density calculation).

2.2. Electroless chemical dealloying of copper-aluminum

The dealloying process yields a large amount of hydrogen production and generates heat because of this exothermic reaction. Heat has deleterious effects such as triggering thermal runaway, reactant spillage and inducing thermal coarsening of the porous metal structure. To control heat generation, protocols were developed in our lab. To prepare an alkaline bath for dealloying, 18 g of solid pure NaOH pellets (ACS reagent, >97.0% from the vendor Sigma-Aldrich) were dissolved in 50 mL of DI water via stirring until the solution became homogenized. Subsequently, DI water was added to fill the beaker to a total volume of 150 ml. A thermocouple was placed inside the beaker to monitor the bath

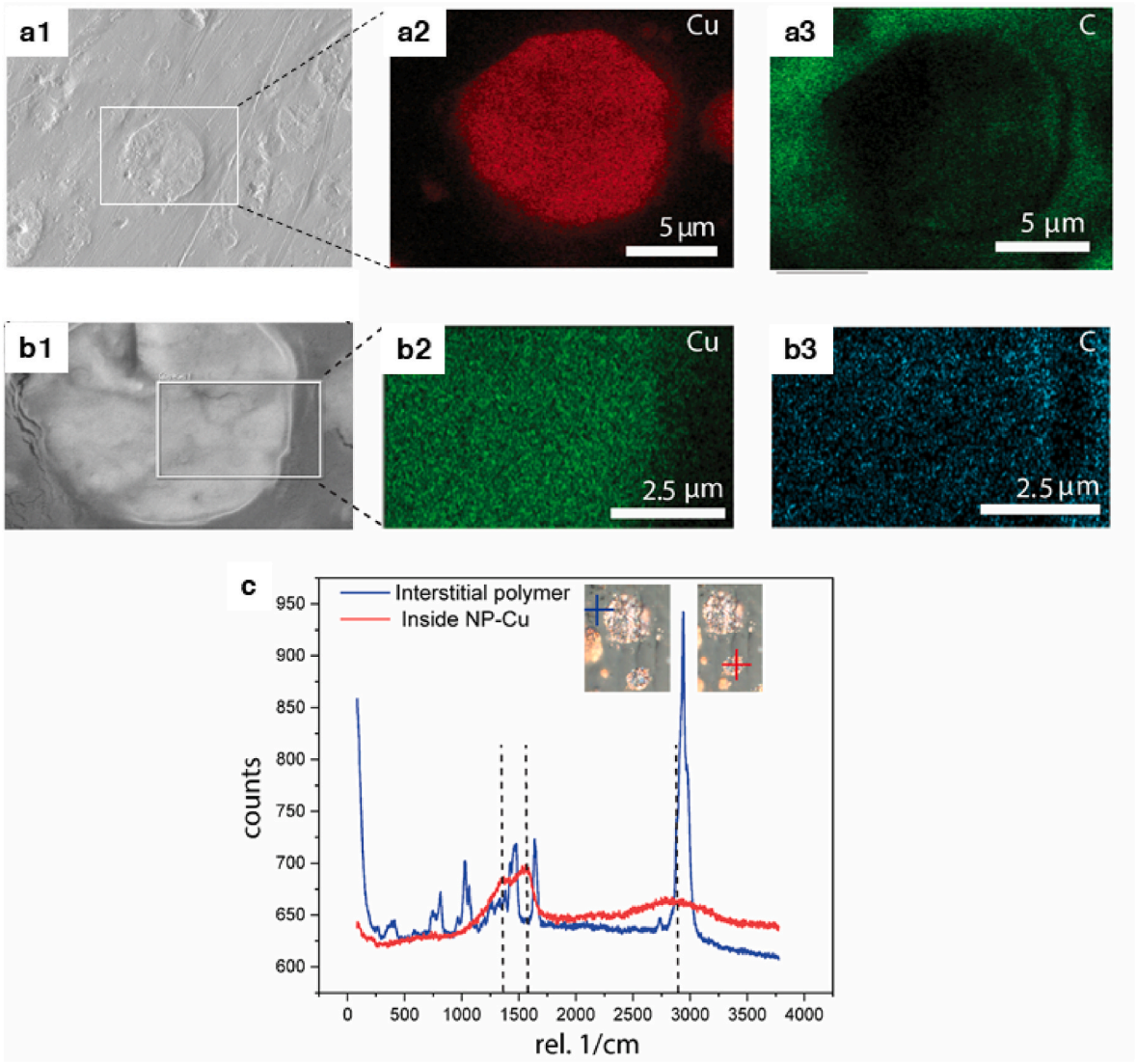

Fig. 3. (a1) SEM image of the mirror polished cross-sectional facet of the composite block and (a2) EDS mapping of a full-size NP-Cu powder imbibed with Aquazol 5k g/mol showing elemental Copper and (a3) Carbon distribution, (b1) magnified SEM image of the mirror polished cross-sectional fact of the composite block, (b2) EDS mapping of the same showing the Cu and (b3) C distribution from the metal-polymer interface to the powder core, (c) overlaid Raman spectra of aquazol in the interstitial region between two NP-Cu powders and Raman spectra inside the NP-Cu pores.

temperature. The beaker was placed on a hot plate in room temperature and a magnetic stirrer was set to rotate at 100 rpm. Next, a total of 15 g of precursor CuAl was added to the solution with an increment of 1.5 g every minute. The temperature was kept below 90 °C at all times with an average temperature of ~70 °C. After dealloying and turning off the magnetic stirring, powders sink to the bottom of the beaker, the solution was decanted from the beaker and the dealloyed powders were washed with DI water. Additional 3–5 cycles of solution decanting and fresh DI water addition were performed. Note that powders were never allowed to dry during the cycles of decanting. Powders were then transferred to another beaker by squirting DI water and the excess DI water was decanted from the top. After that, the wet powders were washed with anhydrous ethanol and the excess ethanol was carefully decanted out from the top by using a pipette. The powders (still in wet condition by alcohol) were then transferred to the vacuum oven (Vendor: Across International | 1.9 Cu Ft) and kept there at a negative 30 in Hg (negative 760 mm Hg) pressure for drying at 100 °C for a minimum of 12 h and a maximum of 24 h. Our lab-scale NP-Cu production process steps from precursor CuAl were shown in Fig. 1a and before and after dealloying operation, powders were shown in Fig. 1 (b) and (c). Next, the chamber was vented to the atmosphere, and powders were allowed to oxidize. During this step, samples exhibited a maximum temperature of 35 °C yielding a high surface area of 14.4 m^2/g and an average pore diameter of 8.4 nm by NaOH dealloying. The pore morphology data were obtained from BET analysis using Micromeritics TriStar II Plus Version 3.03. Oxidized powders were then analyzed by XRD and it was found that the alkaline dealloying process yielded around 15% Cu (II)oxide (Fig. 1 (d)). EDS mapping of dealloyed NP-Cu showed minimal amount of Al left after dealloying operation. After dealloying, porous Cu also underwent volumetric shrinkage as Al etched away creating voids. This shrinkage was computed and details about shrinkage estimation can be found in the supplementary Section A (Figs. S1–4).

2.3. Mixing and composite fabrication

Composite suspension feedstocks were prepared by solution mixing the polymeric solution with metal powders (Figs. 2, 3 and 5 (a)) using a predefined protocol developed by the author in their earlier publication [18]. A modified protocol was made to avoid bubble trapping inside the sample (explained later in this section). The “no air bubble formation”

inside the composite sample was confirmed by grinding and mirror polishing the cross-sectional facets of the samples followed by SEM images (Fig. S11). Initially, Aquazol was dissolved in ACS reagent, 99.5% pure ethanol (Vendor: Sigma-Aldrich) with a 1:10 (w/v) ratio with an initial concentration of 4 g/mL. The magnetic stirring rate was maintained at 100 rpm and low heating (80 °C) was employed on the hotplate with the beaker top covered with aluminum foil until the polymers were fully dissolved to reduce the air trapping during mixing turbulence. After an hour, when the polymers were completely dissolved, and the solution concentration became 6 g/mL, pre-weighed dealloyed and oxidized nanoporous Cu powders (20 vol% considering no imbibition) were gradually added to the polymeric solution. When the porous metal powders and polymers were well mixed in half an hour and a homogenous composite suspension was formed, the beaker was taken into the vacuum oven to keep there at 80 °C for 20 min at a negative one atmospheric pressure (negative 30 inches Hg). The top aluminum foil cover was still maintained inside the vacuum oven to avoid any unwanted solution spillage from the beaker and a 3 mm hole was created in the center of the aluminum foil to facilitate solvent evaporation. After 20 min, the suspension mix was taken back to the hot plate again for stirring an additional 30–35 min reaching the concentration to 8 g/mL. At this point it was taken into the second round of vacuum drying for 20 min and after that, it was taken back to the hot plate for additional stirring. When the suspension becomes more viscous and reach the final concentration of 12 g/mL the suspension was decanted to silicone molds with one-inch cavity and the molds were taken to the vacuum oven to keep there under vacuum for an additional 20 min at 80 °C temperature. At this point, most of the alcohol was evaporated (the boiling point of ethanol is 78 °C at atmospheric pressure) and a thin elastic skin was formed on the molded suspension. A thin glass rod was used to mechanically break and agitate the skin to ensure no remaining ethanol stays inside the mold and to avoid any bubble formation. When the suspension settled, and no more skin formation was observed, the thick suspension was heated to reach 180 °C. Note that Aquazol is an amorphous polymer and it completely softens at180 °C (DSC and TGA curve of Aquazol is provided in Fig. S9). After reaching the desired temperature the suspension inside the mold was kept under vacuum for an additional 2 h to assist imbibition driven by annealing and vacuum impregnation. After 2 h, the vacuum was released, and the suspension was kept in the oven for an additional hour with atmospheric pressure before taking out the mold from the oven to keep it inside the fume hood overnight for natural drying to get the final solidified composite blocks for our density and rheology test and microstructural analysis.

2.4. Extrusion

Extrusion was performed at 180 °C (both heaters at the same temperature) in a desktop single screw extruder ("Noztek Touch" manufactured by Noztek) with a standard dual PID and variable motor speed control. Before the extrusion, the composite suspension was prepared following the same protocol as described in the earlier section. However, in this case composite suspension was transferred to a bigger mold to be dried and solidified and then cleaved manually by a mechanical snipper (Crescent Wiss 9–3/4″ Metal Master® compound action straight and right cut aviation snips) to get the final composite feedstock with an average size of 2.5 mm. The extruder motor speed was maintained at 40 rpm and the extrusion-die internal diameter was 2.85 mm with a minimal (avg. 5%) swelling. Upon extruding, all the filaments passed above a small fan which lowered the filament temperature, and then filaments were winded in a 100 mm diameter spool which was kept at a one-foot distance from the extruder die. All filament extrusions were carried out following a standard protocol [18] as mentioned in our previous article, including (i) frequent cleaning, (ii) free-running before and after the extrusion, and (iii) weekly deep cleaning to avoid any particle accumulation inside the extruder barrel.

2.5. 3D printing

1 cm^3 cube with 30%, 40%, and 50 vol% porous metal was 3D printed with a layer thickness of 0.2 mm, infill density 100%, and print speed of 20 mm/s using our desktop 3D printer Ultimaker Cura 2. The glass printing bed was preheated to 71 °C and the initial layer height was tripled to ensure good adhesion with the base layer. The detailed 3D printing parameters are listed in the supplementary section Table S1.

2.6. Tests and characterizations

2.6.1. Wettability test

Contact angle and surface tension tests were performed at three different concentrations (solution concentration 6 g/mL, 8 g/mL, and 12 g/mL) for all molecular weights of aquazol on the surfaces of a tightly packed bed of dealloyed porous Cu. SDC-350 inclination optical contact angle meter (manufactured by Dongguan Shengding Precision Instrument Co. LTD) was used to perform all the contact angle and surface tension tests. The apparatus was equipped with a professional-grade high-precision injection system with the lowest droplet control accuracy of 0.01 μl and an adjustable brightness of the LED cold light source system. Multiple contact angle measurements were carried out and a representative contact angle was taken with a measurement accuracy of ±0.1°. The instrument's other features (i.e. an automatic surface tension calculator using the solution pendant drop's image and an image streaming option to capture continuous images at a 0.1-s frequency) were also utilized in our study. Dealloyed nanoporous Cu powders were placed in a mold and mechanically pressurized to get a tightly compact powder bed as a substrate for the wettability test. The polymeric solution concentrations were increased gradually by evaporating the solvents and subsequent contact angles were taken accordingly as a function of increasing concentration. Contact angles for different Aquazol of the initial concentration (6 g/mL) were analyzed (the streaming digital images of the advancing droplet through the powder packed bed were captured and analyzed by the ImageJ software) as a function of time to understand the imbibition kinetics.

2.6.2. BET measurement

Brunauer–Emmett–Teller (BET) analysis of porous copper powders was performed on Tristar II Plus (Micromeritics Instruments Corporation). First, powders were weighed in a glass vial so the mass of analyzed powders is ~ 2–3 g. Next, the vials filled with powders were transferred to VacPrep degassing station for 3 h at 80 °C using Ar gas. Further, the vials were attached to Tristar II Plus using a clamp and vacuum is applied. After this, the system submerged the vial to liquid nitrogen. Lastly, by purging nitrogen gas into vials, the specific surface area and pore size distribution of NP-Cu powders were derived.

2.6.3. Density test

Density measurement was carried out for each Mw of Aquazol after making the composites with dealloyed nanopowders (three samples for each composite). For each M_w of Aquazol, three samples were tested, and five measurements were taken for each. The average densities and standard deviations were calculated from the measured data. The density test was conducted based on Archimedes' principle in AD-1654 density determination kit with an advanced electronic balance with an accuracy of up to four decimal points. Instead of water mineral oil ($\rho = 0.87$ g/cm^3) was used as a submerging liquid for this test since our Aquazol could be dissolved by water.

2.6.4. Rheology test

Rheological tests were performed after melting the molded solid composite block. Before conducting the test, samples were grinded and mirror-polished in one facet down to 0.1 μm to ensure samples were without bubbles entrapped inside it. 180 °C temperature was chosen for Aquazol to be completely melted to measure the dynamic viscosity. For

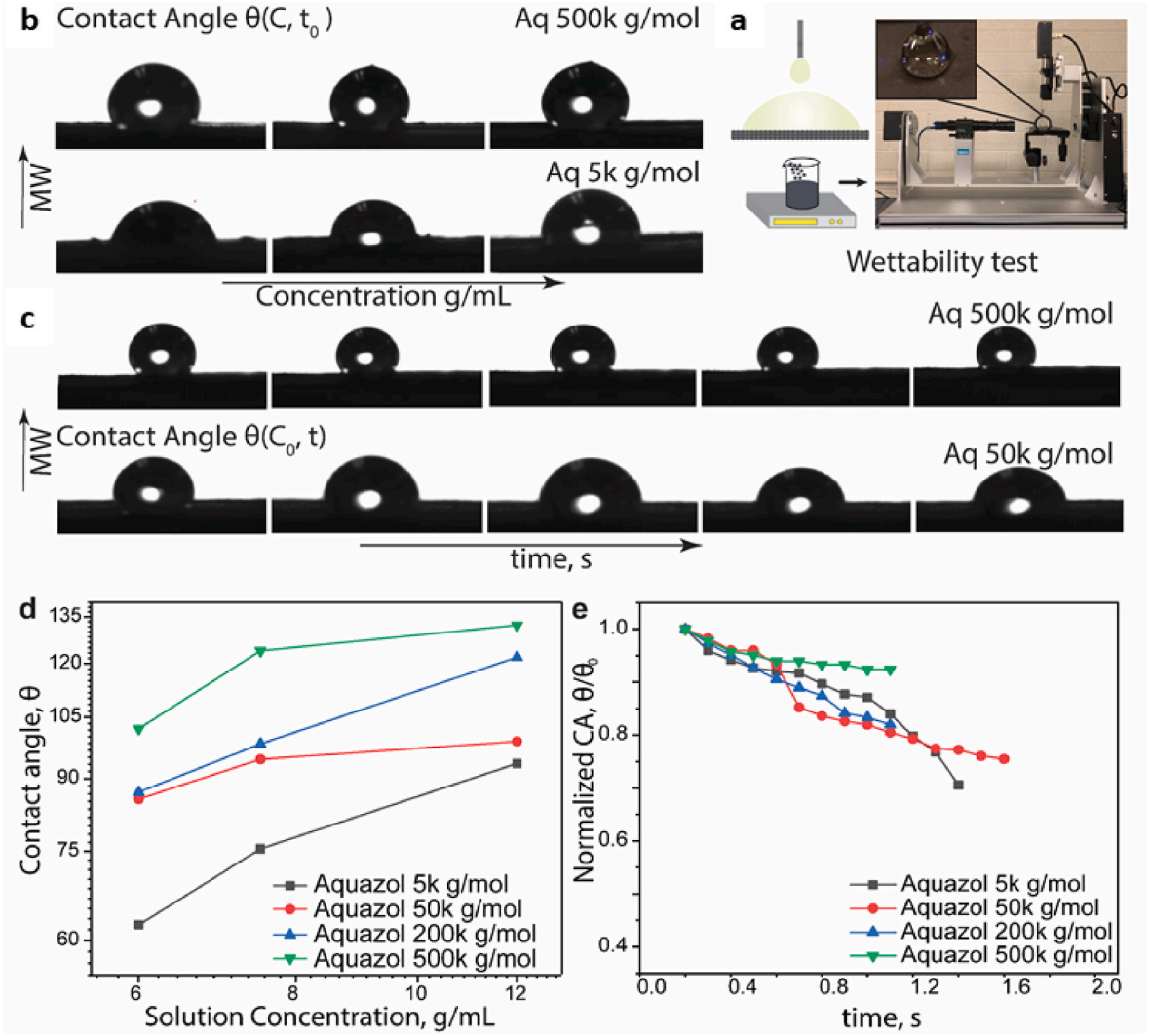

Fig. 4. (a) wettability test set up and polymeric fluid droplet cast on the NP-Cu powder bed (inset), (b) Contact angles (at t = 0s) of polymeric fluid (dissolved aquazol in ethanol) as a function of concentration from 6 g/ml to 12 g/ml, (c) contact angles of polymeric fluid (at C═C$_0$)as a function of time through the packed NP-Cu powder bed, (d) contact angle curves of different M_w aquazol solution droplets as a function of concentration (at t = 0s), (e) contact angle curves of advancing droplets of different Mw samples through the packed bed as a function of time (at C═C$_0$).

each test, solid composite blocks were broken and melted in a vacuum oven, and then the composite melt sample was placed inside a rotational rheometer (DHR 2 manufactured by TA instrument) on a 25 mm parallel plate with a 400 μm gap size. Each sample was pre-soaked for 10 min and a shear rate range of 2.8 × 10-3 s^{-1} to 1000 s^{-1} was used to conduct the flow sweep rheology test.

2.6.5. *X-ray powder diffraction (XRD)*

For phase characterization of the porous copper powder and their present phases, samples were analyzed by X-ray diffraction (XRD, Malvern Pan analytical Aeris, Research Edition), equipped with a Cu-Kα source emitting radiation of 1.54060 Å wavelength. Data collection for diffraction patterns was acquired within a 10–100° 2θ scanning range, with 18.87 s per step, and step size defined as 0.0110°.

2.6.6. *Microscopic characterization*

Metal nanofoams were seen under Scanning Electron Microscopy (SEM) to find microstructural difference before and after dealloying. Powders were also analyzed via Energy Dispersive Spectroscopy (EDS) to see the mapping of Cu, Oxygen and any residual Al left with the dealloyed powders. Apart from that, for each composite block one cross-sectional facet was grinded and mirror polished down to 0.4 μm to undergo SEM and EDS mapping. EDS mapping was intended to see the elemental carbon infiltration from the boundary of each porous wall from the interstitial region to the pores. Each sample was gold-coated up to 10 nm to increase the conductivity of the sample for SEM analysis. All top-down cross-sectional images and EDS were carried out in Auriga SEM manufactured by Zeiss. For the confocal Raman spectroscopy, a green laser with a wavelength of 532 nm and 0.8 mW laser power was used. The image taken with a laser spot size if 0.3 μm at the 100x magnification.

3. Results and discussions

In this work, PMCs were formed with spherical nanoporous copper powders at high-loadings (~47–68.9 vol%) to demonstrate their extrudability into filaments and their 3D printability via FFF in a similar approach to metal FFF [18] which includes dissolving the polymer phase in a solvent, mixing NP-Cu into it, drying the solvent at 80 °C and annealing it at 180 °C (Fig. 2). However, in the case of porous fillers, the polymer matrix in its melt or solution state can partially or fully imbibe inside the porous metal by capillary action which can increase the packing volume fraction of the powders in the composite, which is known to alter their viscoelastic behavior and extrusion performance

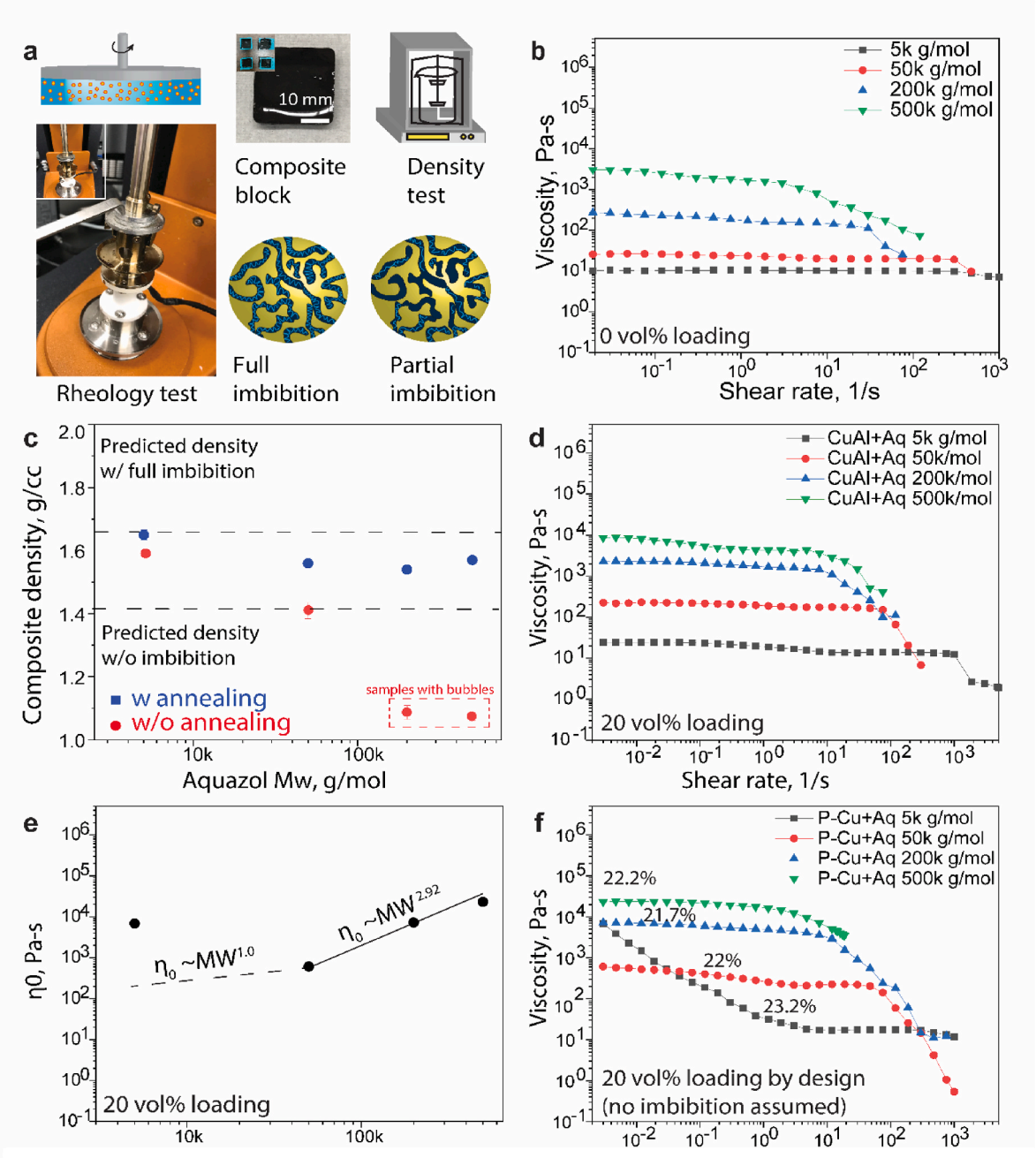

Fig. 5. (a) Flow sweep rheology test setup, schematic of the density test setup, a sample composite block and a cartoon of NP-Cu powders with two different degree of imbibition possibility by the infiltrating polymer, (b) dynamic viscosity vs. shear rate of pure aquazol melt at 180 °C, (c) composite block density as a function of M_w with and without the annealing steps, (d) dynamic viscosity vs. shear rate of composite melt made of 20 vol% of precursor CuAl at 180 °C, (e) zero-shear viscosity correlation as a function of polymer M_w with 20 vol% NP-Cu loading, and (f) dynamic viscosity vs. shear rate of composite melt made of 20 vol% NP-Cu powders at 180 °C.

[18,32–34]. In regard to the metal host, several factors can regulate imbibition, such as the tortuosity of the porous channels, their surface roughness and surface passivation. On the polymer side, it can be regulated by polymer-substrate interaction in the presence of different solvents [35], their wettability characteristics and contact angle [36–40], its melt rheology which widely depends on the polymer selection and concentration, and the relative size of the radius of gyration (R_g) of the polymer and the pore diameter [41–45] as the latter represents a physical barrier. Finally, the fluid confinement within the nanopores can alter the macroscopic properties (e.g., viscosity) of the polymeric phase through effects such as interfacial interaction [23], segmental relaxation [42] and topological interaction [46]. Among all of these possible mechanisms, this study focused its attention on the effects of polymer chain radius of gyration has in regulating its imbibition into the nanopores. Imbibition took place in three steps: (i) capillary infiltration when NP-Cu powders are first dispensed in the polymer solution dissolved in Ethanol (Fig. 2a and c – step 1), (ii) solvent-polymer exchange process performed above the boiling point of the solvent (i.e., 80 °C) in vacuum (Fig. 2c – step 2) and (iii) an annealing step above the melting temperature of the polymer (Fig. 2c – step 3). To determine the contributions of each step to the imbibition of the polymer and its densification, this paper (a) presents physical evidence of imbibition via EDS and Raman mapping of the polymer phase within the pores, (b) measures the wettability of polymer solutions into metal powders

associated with step-i and (c) the density of the composite both before (step-ii) and after the annealing procedure (step-iii). As part of the effort (a), EDS (See Fig. 3a–b) and Raman spectroscopy (See Fig. 3c) were employed to analyzed the mirror-polished cross-section of the composite after step-iii. In both EDS and Raman mappings, evidence of amorphous C was found in the core of the porous powders. For the Raman data, peaks at 1341 cm^{-1}, 1522 cm^{-1} and 2850 cm^{-1} (Fig. 3c) were observed corresponding to amorphous carbon [47,48] confirming the presence of the polymer within its pores. Peaks were broad due to the metal fluorescence. The lack of peaks associated with bonding present in aquazol is associated with the polishing step which altered the microstructure of the polymer.

When mixing dissolved polymer solutions with the nanoporous powder, it is a necessary condition for wetting to take place if the powder is to be impregnated with it. To determine that, a wettability test (Fig. 4) was carried out in which polymer solutions of different concentrations (i.e., different solvent-polymer ratios) were drop cast onto powder beds of the nanoporous copper powder. As the droplet was cast, it was absorbed into the powder bed at rates that depend on its initial concentration and molecular weight. Thus, the contact angle formed between air, the powder bed, and the polymer solution were recorded as soon as the droplet is cast (i.e., t = 0) (Fig. 4a) and monitored in time (i.e., θ(t)) (Fig. 4c). As evident from Fig. 4d, high molecular weight samples (i.e., 500 g/mol) produce non-wetting contact angles at t = 0 with increasing angles at higher polymer concentrations which do not favor imbibition of the polymer solution. In contrast, low molecular weight samples (i.e., 5 g/mol) exhibit wetting contact angles (i.e., <90°) at all polymer concentrations tested. This result suggests that mixing of polymer solutions with metals at sufficiently low concentrations guarantees imbibition conditions were met with the exception when molecular weight was 500 g/mol. In Fig. 4e, dynamic contact angles normalized by θ_o of the advancing droplet through the packed metal powder bed were plotted. It was noticeable that the normalized contact angle of samples with MW of 500k g/mol experienced an approximate 5% decrease with time which is significantly less than the samples with MW of 5k g/mol that yielded a 30% decrease, suggesting the latter became more wetting as the droplet settled on the surface. These graphs along with the visual evidence serve as proof of how the imbibition kinetics was impacted by molecular weight which fortified our previous claim that the lower the molecular weight polymers (shorter polymer chain R_g) shows faster the imbibition through the nanopores in step – 1 (Fig. 2c).

Once porous powders were wet with polymer solutions, the composite underwent a phase inversion as it was dried with the solvent exchanging with the polymer at 80 °C. In this step, polymer chains get densified inside the nanopores driven by the polymer concentration difference between exterior and interior domains of NP-Cu. This process was governed by capillarity and diffusional processes and were expected to depend on the relative size of Rg (which ranges from 2 nm to 20 nm depending on molecular weight) and the average pore diameter (i.e., 22 nm). With further annealing at 180 °C above its melting temperature, the polymer's mobility increased due to the enhanced segmental dynamics under high thermal energy, making it more prone to imbibition, diffusional transport and densification (Fig. 2c – step 3). To quantify the degree of densification during these steps, a density test (Fig. 5a) was performed on the composite after steps (i-ii). When the polymer imbibes into the nanopores, the composite's density should increase as it replaces the pores. After step (ii), the density of MW 50k, 200k, and 500k were within the error bar of the density measurement with only the MW 5k g/mol being distinctively 7% higher than the average of other molecular weights, suggesting the latter experienced a greater degree of imbibition after step 3 (Fig. 2c). For reference, theoretical densities of extreme cases were included in Fig. 5 (see supplementary Section A for the detailed calculation) for when (a) pores were completely imbibed by polymers (i.e., 1.41 g/cm^3) and (b) no imbibition of polymers took place into the pores (i.e., 1.642 g/cm^3). The theoretical densities were calculated using the following equation:

$$\rho_{composite} = \frac{m_{aq} + m_{metal}}{V_{aq} + V_m + V_{pores}^{unfilled}} = \frac{m_{aq} + m_{P-Cu}}{\frac{m_{aq}}{\rho_{aq}} + \frac{m_{P-Cu}}{\rho_{true}^{P-Cu}} + m_{P-Cu}\left(\frac{1}{\rho_{skel}^{P-Cu}} - \frac{1}{\rho_{true}^{P-Cu}}\right)(1 - X)} \quad (3)$$

Where, m_{Aq} and m_{metal} are the as design weight of the polymer and nanoporous Cu powders and V_{aq}, V_m, $V_{unfilled\ pores}$ are the calculated volume of the polymer, metal and unfilled pores inside the nanoporous Cu. For example, the increase in density between 200k and 5k g/mol samples of 20 vol% translates to an increase in the packing factor of the powder from 21.7 vol% to 23.2 vol% (Fig. S12). This improved imbibition is attributed to the small radius of gyration of MW 5k g/mol (i.e., 2 nm) relative to the average pore size of the nanoporous metal (i.e., 22 nm) which reduced the physical and entropy barriers for imbibition. After step (i), the densities of the composites were also measured to distinguish the contributions of each step. Samples with MW 200k and 500k g/mol exhibited entrapped gas bubbles (Fig. S10) after step 1 making it hard to draw any conclusions. However, samples with MWs 5k and 50k were bubble-free and their density change was found to be 4% and 11% higher after annealing, respectively. Note that Table S2, Table S3, and supplementary Section A and Section B detail the calculations for the fill fraction of polymers and the packing volume fraction of porous powders inside the polymer matrix. According to our density data the fill fraction is almost 72% for MW 500k g/mol and 103% for the 5k g/mol. This result highlights the relevance of the annealing step in supporting higher degrees of imbibition even when contact angle was not favorable (>90°). Bubbles were eliminated after the vacuum annealing step (ii) for all samples (Fig. S11). The density difference between fully annealed samples of 5k g/mol and 50k g/mol was found to be 6% which is equivalent to the fill fraction change of 36.4% and NP-Cu powder packing volume fraction change of 1.5 vol% (see supplementary Section A, particularly Fig. S12,Table S2 for additional details).

The rheology of suspensions is governed by two interacting forces: (i) the hydrodynamic effect and (ii) particle-particle network force interactions [49]. The latter dominates as the particle packing volume fraction approaches closed-packed values as low as 10 vol% to 40 vol% (depending on the suspension) [[50,51]]. For example, if the packing volume fraction of porous copper powders increases due to imbibition, the Krieger-Daughtery analytical model [88] predicts an increase in zero-shear viscosity. In Fig. 5b, dynamic melt viscosity of the pure aquazol was measured and compared with the melt viscosities of aquazol mixed with solid Cu–Al powders (Fig. 5d) and aquazol-NP-Cu composite (Fig. 5f) at 20 vol% loading to quantify the rheological differences. Note the latter samples had a 20 vol% loading if imbibition was not considered, but after density measurements, their actual a loading range was found to be in between 21.7 and 23.2% (Table S3 and Fig. S12). It was clear that both at the low and high shear rates, the NP-Cu composite exhibited higher viscosities than its solid counterpart and the pure aquazol, highlighting its thickening due to imbibition, densification and particle reinforcement. A distinctive signature of NP-Cu composite with 5k g/mol was an increase in its zero-shear viscosity and shear-thinning at low shear rates, and a linear viscoelastic plateau at high shear rates (Fig. 5f). In regard to the zero shear viscosity, it is expected in a polymer or a composite to scale as $\eta_0 \propto MW^{1.0}$ at shorter chain lengths, and as $\eta_0 \propto MW^{3.4}$ at chain lengths greater than a critical molecular weight (Mc) [52] which can be calculated from the storage modulus plateau of the melt polymer [53]. In Fig. 5e, the zero-shear viscosity scaling of NP-Cu and solid composites were shown with $\eta_0 \propto MW^{2.92}$ at the high MW range. In the same figure, the zero-shear viscosity of composite melt made of 5k g/mol deviated significantly from the theoretical $MW^{1.0}$ scaling. The relatively small addition in the packing factor of Aquazol-NP-Cu (i.e., 23.2 vol% for MW 5 g/mol) relative to Aquazol-CuAl (i.e., 20.0 vol%) may not be the only explanation for such large changes in its rheology. In fact, other

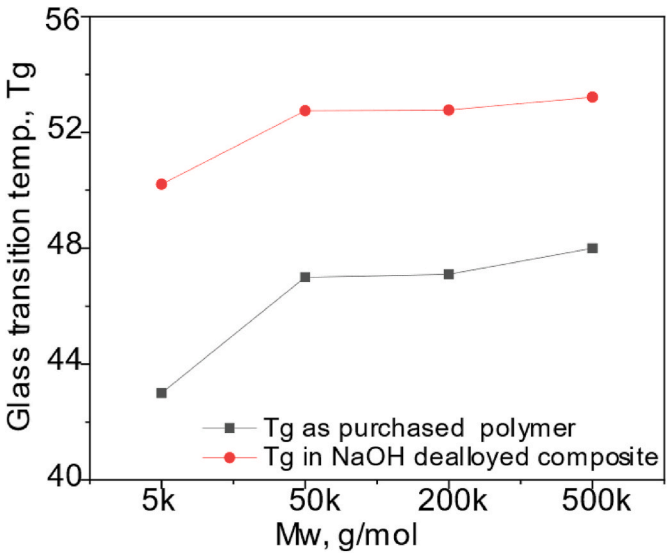

Fig. 6. Glass transition temperature (Tg) variation as a function of polymer MW of pure polymer and Np-Cu-Aquazol composite at powder concentration of 20% by volume.

explanations such as its reduced particle size (owning to powder shrinkage during dealloying) and its effect on viscosity [54], and enhanced drag force with decreasing distance between particles [55], leading to an increase in their coagulation kinetics [56] and melt viscosity had been found in literature. Granick [57] demonstrated that the effective shear viscosity of the infiltrating polymers inside the porous wall increases as a result of slowing chain relaxation compared to the bulk. Albeit not ruled out, no evidence in our case suggests that the polymer chains were in nanoconfinement within NP-Cu, which were expected to have an increased viscosity [57], contributed to the overall viscosity specially if one assumes them static within the pores.

There has been evidence [42,44,58–62] that polymer nanoconfinement affects the segmental dynamics and glass transition properties in PMC. While nanoconfined inside porous metal architecture, increased topological constraints can perturb the segmental chain dynamics of polymer chain and limit the chain entanglement [44,59,63] leading to more tough materials with high glass transition temperature [42,58,64]. In our study portrayed in Fig. 6, for all the composites made of different molecular weight polymers experienced an increase in their glass transition temperature (T_g) when compared with the corresponding T_g of the pure polymer. The most distinguishable T_g increase was found in the composite sample made with the lowest M_w polymer (5k g/mol), in which the fill fraction was the highest. The increase in T_g points out to the effect of spatial nanoconfinement on slowing down the segmental dynamics of bound polymers which was mentioned in many literatures [43,62]. Despite evidence of nanoconfinement effects, there was substantial amounts of polymer at interstitial regions between the nanoporous metal powders which raised questions if the nanoconfined polymer inside the pores played any role in the macroscopic rheology of the composite or if the unconfined polymers were the dominant lubricant between powders when the melt was being sheared. Further research is needed to elucidate this point.

Additionally, a 3D printed composite was manufactured via fused filament fabrication (Fig. 7). Rather than making the composite in block via molding and casting, the solution mixed black paste was dried and cut to make our customized feedstock for FFF. The feedstock (Fig. 7d) was then fed into the extruder hopper to extrude PMC filament (Fig. 7e) and, finally, they were 3D printed in a desktop FFF printer (Fig. 7f). The full imbibition of nanopores filled by the lowest MW samples (i.e. 5k g/

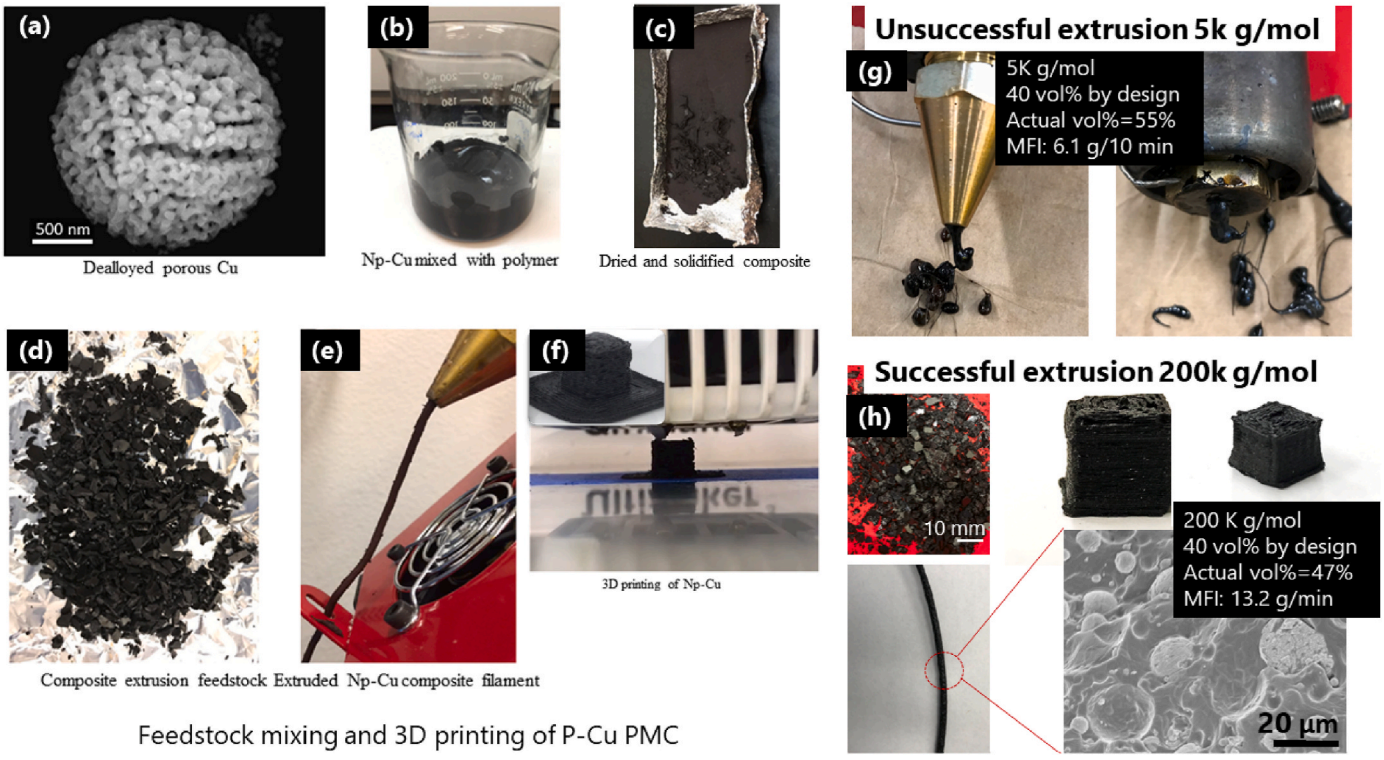

Fig. 7. Feedstock mixing and 3D printing process of PMC-NP-Cu: (a) dealloyed NP-Cu, (b) NP-Cu mixed with Aquazol dissolved in ethanol, (c) dried and solidified composite, (d) mechanically cleaved custom made PMC-NP-Cu feedstock, (e) extruded filaments of 40 vol% NP-Cu, (f) 3D printing of PMC-NP-Cu and a 3D printed part with 40 vol% NP-Cu assuming no imbibition (inset), (g) low melt flow and extrusion failure due to internal jamming of Aquazol 5 kg/mol, because of full capillary imbibition packing vol% reached 55% from the design packing factor of NP-Cu (40 vol%), and (h) successful extrusion of Aquazol 200k g/mol where packing reached 47 vol% (mixing design value NP-Cu = 40 vol%).

mol) led to packing factor increase by 15 vol% resulting a jamming inside the barrel (Fig. 7g) with very low melt flow index (MFI) (~6 g/10 min) compared to moderate (>10g/10 min) MFI (Fig. 7h) for the sample with 200k g/mol (which had around ~60 vol% fill fraction compared to 100% fill fraction of 5k g/mol sample, Fig. S12). The packing fraction increase was calculated using the following the developed formula (the detailed calculation is listed in supplementary section a):

$$V_m^X = \frac{V_{P-Cu}}{V_m + V_{aq} + V_{pores}^{unfilled}(1-X)} \quad (4)$$

Where, V_m^X is the volumetric packing% of nanoporous Cu with the fill fraction of x%, $V_{p\text{-}Cu}$,V_m, V_{aq} and $V_{unfilled\ pores}$ are the calculated volume of porous Cu, only metallic portion volume, volume of polymer and the unfilled pore volume respectively. This phenomenon of actual metal powder packing fraction increase, inside the polymer matrix based on the degree of imbibition gives us both qualitative and quantitative insight on how capillary imbibition can lead to extrusion failure via jamming. Our study could be used as a deterministic tool to design new materials including selecting the right MW polymer to be solution mixed with NP-Cu for a successful extrusion and 3D printing. Also note that it is possible that a disruption of the entanglement network may occur at low molecular weights (e.g., 5k g/mol) further undermining the elongational flow.

4. Conclusion

Nanoporous metals have unique physiochemical properties because of their inherent ligament size enabling their application in high surface area electronics with diffusional pathways. Here we reported FFF based 3D printing process of PMC-NP-Cu with high fill fraction of NP-Cu and ways to avoid jamming during extrusion which was originated from capillary imbibition. To accomplish that, the role of capillary imbibition of polymers into metal nanopores was investigated to understand its effect on melt rheology, density and volumetric packing fraction of nanoporous metal in the polymer matrix to enable its continuous extrusion and 3D printing. It was demonstrated that the polymer M_w or R_g, ultimately dictates its zero-shear viscosity and shear thinning response, which consequentially facilitates or inhibits capillary-driven imbibition and densification of pores. Finally, a comparative analysis of higher imbibition prone polymer (with shorter chain length or R_g) vs. lower imbibition prone polymer (higher chain length or R_g) was studied via extrusion, where small R_g polymers were found to experience extrusion failure by jamming due to the combined effect of higher volumetric metal packing and nanoconfinement, but the later succeeded extrusion and continuous printing at higher volumetric metal content (>50 vol% by design). This study provided a deterministic tool for a successful materials design for FFF based extrusion and 3D printing involving conductive nanoporous metals with high surface area for any thermoplastic binder, which could be a steppingstone towards low cost manufacturing of 3D printed electronics.

Declaration of competing interest

The authors declare the following financial interests/personal relationships which may be considered as potential competing interests: Dr. Bruno Azeredo co-owns a start up called Nanobionics, LLC which conducts work in the area of nanocoatings for dental prosthetics which is not related to the subject of this submission/manuscript.

Data availability

Data will be made available on request.

Acknowledgment

We gratefully acknowledge the use of facilities within the LeRoy Eying Center for Solid State Science, and the John M Cowley High-Resolution Electron Microscopy Center at Arizona State University. We acknowledge Professor Dhruv Bhate to allow us performing the density test in his lab and, last but not the least, we acknowledge the staff of the ASU Innovation Hub (namely, Scott Almen, Rhet Sweeney, and Cameron Noe) for facilitating our microscopic and surface finishing tasks. The authors acknowledge also financial support from the NSF CMMI Grants No. 1932899.

Appendix A. Supplementary data

Supplementary data to this article can be found online at https://doi.org/10.1016/j.compositesb.2023.110913.

References

[1] Juarez T, Biener J, Weissmüller J, Hodge AM. Nanoporous metals with structural hierarchy: a review. Adv Eng Mater 2017;19:1–23. https://doi.org/10.1002/adem.201700389.
[2] Detsi E, De Jong E, Zinchenko A, Vuković Z, Vuković I, Punzhin S, Loos K, Ten Brinke G, De Raedt HA, Onck PR, De Hosson JTM. On the specific surface area of nanoporous materials. Acta Mater 2011;59:7488–97. https://doi.org/10.1016/j.actamat.2011.08.025.
[3] Fujita T, Guan P, McKenna K, Lang X, Hirata A, Zhang L, Tokunaga T, Arai S, Yamamoto Y, Tanaka N, Ishikawa Y, Asao N, Yamamoto Y, Erlebacher J, Chen M. Atomic origins of the high catalytic activity of nanoporous gold. Nat Mater 2012;11:775–80. https://doi.org/10.1038/nmat3391.
[4] Zou L, Ge M, Zhao C, Meng Q, Wang H, Liu X, Lin CH, Xiao X, Lee WK, Shen Q, Chen F, Chen-Wiegart YCK. Designing multiscale porous metal by simple dealloying with 3D morphological evolution mechanism revealed via X-ray nano-tomography. ACS Appl Mater Interfaces 2020;12:2793–804. https://doi.org/10.1021/acsami.9b16392.
[5] Bhattacharya A, Calmidi VV, Mahajan RL. Thermophysical properties of high porosity metal foams. Int J Heat Mass Tran 2002;45:1017–31. https://doi.org/10.1016/S0017-9310(01)00220-4.
[6] Huang A, He Y, Zhou Y, Zhou Y, Yang Y, Zhang J, Luo L, Mao Q, Hou D, Yang J. A review of recent applications of porous metals and metal oxide in energy storage, sensing and catalysis. J Mater Sci 2019;54:949–73. https://doi.org/10.1007/s10853-018-2961-5.
[7] Keum H, Carlson A, Ning H, Mihi A, Eisenhaure JD, Braun PV, Rogers JA, Kim S. Silicon micro-masonry using elastomeric stamps for three-dimensional microfabrication. J Micromech Microeng 2012;22. https://doi.org/10.1088/0960-1317/22/5/055018.
[8] Arpin KA, Pikul JH, King WP, Fan H, Braun PV. Template directed assembly of dynamic micellar nanoparticles. Soft Matter 2011;7:10252–7. https://doi.org/10.1039/c1sm06078c.
[9] Jiang Z, Pikul JH. Centimetre-scale crack-free self-assembly for ultra-high tensile strength metallic nanolattices. Nat Mater 2021;20:1512–8. https://doi.org/10.1038/s41563-021-01039-7.
[10] Vyatskikh A, Delalande S, Kudo A, Zhang X, Portela CM, Greer JR. Additive manufacturing of 3D nano-architected metals. Nat Commun 2018;9. https://doi.org/10.1038/s41467-018-03071-9.
[11] Pikul JH, Gang Zhang H, Cho J, Braun PV, King WP. High-power lithium ion microbatteries from interdigitated three-dimensional bicontinuous nanoporous electrodes. Nat Commun 2013;4:1–5. https://doi.org/10.1038/ncomms2747.
[12] Zhu C, Qi Z, Beck VA, Luneau M, Lattimer J, Chen W, Worsley MA, Ye J, Duoss EB, Spadaccini CM, Friend CM, Biener J. Toward digitally controlled catalyst architectures: hierarchical nanoporous gold via 3D printing. Sci Adv 2018;4. https://doi.org/10.1126/sciadv.aas9459.
[13] Zhang Y, Sun X, Nomura N, Fujita T. Hierarchical nanoporous copper architectures via 3D printing technique for highly efficient catalysts. Small 2019;15:1–7. https://doi.org/10.1002/smll.201805432.
[14] Erlebacher J, Aziz MJ, Karma A, Dimitrov N, Sieradzki K. Evolution of nanoporosity in dealloying. Nature 2001;410:5–8.
[15] Li R, Sieradzki K. Ductile-brittle transition in random porous Au. Phys Rev Lett 1992;68:1168–71. https://doi.org/10.1103/PhysRevLett.68.1168.
[16] Ye XL, Jin HJ. Corrosion-induced strengthening: development of high-strength nanoporous metals. Adv Eng Mater 2016;18:1050–8. https://doi.org/10.1002/adem.201500521.
[17] Chuang A, Erlebacher J. Challenges and opportunities for integrating dealloying methods into additive manufacturing. Materials 2020;13. https://doi.org/10.3390/MA13173706.
[18] Hasib AG, Niauzorau S, Xu W, Niverty S, Kublik N, Williams J, Chawla N, Song K, Azeredo B. Rheology scaling of spherical metal powders dispersed in thermoplastics and its correlation to the extrudability of filaments for 3D printing. Addit Manuf 2021;41. https://doi.org/10.1016/j.addma.2021.101967.

[19] Tao Y, Kong F, Li Z, Zhang J, Zhao X, Yin Q, Xing D, Li P. A review on voids of 3D printed parts by fused filament fabrication. J Mater Res Technol 2021;15:4860–79. https://doi.org/10.1016/j.jmrt.2021.10.108.

[20] Al-Maharma AY, Patil SP, Markert B. Effects of porosity on the mechanical properties of additively manufactured components: a critical review. Mater Res Express 2020;7. https://doi.org/10.1088/2053-1591/abcc5d.

[21] Mariappan DD, Kim S, Boutilier MSH, Zhao J, Zhao H, Beroz J, Muecke U, Sojoudi H, Gleason K, Brun PT, Hart AJ. Dynamics of liquid transfer from nanoporous stamps in high-resolution flexographic printing. Langmuir 2019;35:7659–71. https://doi.org/10.1021/acs.langmuir.9b00460.

[22] Kim S, Sojoudi H, Zhao H, Mariappan D, McKinley GH, Gleason KK, Hart AJ. Ultrathin high-resolution flexographic printing using nanoporous stamps. Sci Adv 2016;2. https://doi.org/10.1126/sciadv.1601660.

[23] Tu CH, Zhou J, Doi M, Butt HJ, Floudas G. Interfacial interactions during in situ polymer imbibition in nanopores. Phys Rev Lett 2020;125:127802. https://doi.org/10.1103/PhysRevLett.125.127802.

[24] Oko A, Martinez DM, Swerin A. Infiltration and dimensional scaling of inkjet droplets on thick isotropic porous materials. Microfluid Nanofluidics 2014;17:413–22. https://doi.org/10.1007/s10404-013-1313-7.

[25] Sahimi M. Flow phenomena in rocks: from continuum models to fractals, percolation, cellular automata, and simulated annealing. Rev Mod Phys 1993;65:1393–534. https://doi.org/10.1103/RevModPhys.65.1393.

[26] Alava M, Dubé M, Rost M. Imbibition in disordered media. Adv Phys 2004;53:83–175. https://doi.org/10.1080/00018730410001687363.

[27] Xue Y, Markmann J, Duan H, Weissmüller J, Huber P. Switchable imbibition in nanoporous gold. Nat Commun 2014;5. https://doi.org/10.1038/ncomms5237.

[28] Kar S, Das SS, Laha S, Chakraborty S. Microfluidics on porous substrates mediated by capillarity-driven transport. Ind Eng Chem Res 2020;59:3644–54. https://doi.org/10.1021/acs.iecr.9b04772.

[29] Flori P. Thermodynamics of high polymer solutions. J Chem Phys 1941;9:660. https://doi.org/10.1007/s12045-017-0481-2.

[30] Flory PJ. Thermodynamics of heterogeneous polymers and their solutions. J Chem Phys 1944;12:425–38. https://doi.org/10.1063/1.1723887.

[31] Huggins M. Revised theory. Phys Rev 1964;40.

[32] Krieger IM, Dougherty TJ. A mechanism for non-Newtonian flow in suspensions of rigid spheres. Trans Soc Rheol 1959;3:137–52. https://doi.org/10.1122/1.548848.

[33] Pabst W. Fundamental considerations on suspension rheology. Ceram. - Silikaty. 2004;48:6–13.

[34] Cassagnau P. Linear viscoelasticity and dynamics of suspensions and molten polymers filled with nanoparticles of different aspect ratios. Polymer 2013;54:4762–75. https://doi.org/10.1016/j.polymer.2013.06.012.

[35] Meybodi HE, Kharrat R, Wang X. Study of microscopic and macroscopic displacement behaviors of polymer solution in water-wet and oil-wet media, 89. Transp. Porous Media; 2011. p. 97–120. https://doi.org/10.1007/s11242-011-9754-5.

[36] Digilov RM. Capillary rise of a non-Newtonian power law liquid: impact of the fluid rheology and dynamic contact angle. Langmuir 2008;24:13663–7. https://doi.org/10.1021/la801807j.

[37] Zhao W, Rafailovich MH, Sokolov J, Fetters LJ, Plano R, Sanyal MK, Sinha SK, Sauer BB. Wetting properties of thin liquid polyethylene propylene films. Phys Rev Lett 1993;70:1453–6. https://doi.org/10.1103/PhysRevLett.70.1453.

[38] Khoryani Z, Seyfi J, Nekoei M. Investigating the effects of polymer molecular weight and non-solvent content on the phase separation, surface morphology and hydrophobicity of polyvinyl chloride films. Appl Surf Sci 2018;428:933–40. https://doi.org/10.1016/j.apsusc.2017.09.235.

[39] Brooks CF, Grillet AM, Emerson JA. Experimental investigation of the spontaneous wetting of polymers and polymer blends. Langmuir 2006;22:9928–41. https://doi.org/10.1021/la061013e.

[40] Dee GT, Sauer BB. The molecular weight and temperature dependence of polymer surface tension: comparison of experiment with interface gradient theory. J Colloid Interface Sci 1992;152:85–103. https://doi.org/10.1016/0021-9797(92)90010-J.

[41] Cimino RT, Rasmussen CJ, Brun Y, Neimark AV. Mechanisms of chain adsorption on porous substrates and critical conditions of polymer chromatography. J Colloid Interface Sci 2016;481:181–93. https://doi.org/10.1016/j.jcis.2016.07.019.

[42] Jin S, McKenna GB. Effect of nanoconfinement on polymer chain dynamics. Macromolecules 2020;53:10212–6. https://doi.org/10.1021/acs.macromol.0c00365.

[43] Bailey EJ, Riggleman RA, Winey KI. Polymer conformations and diffusion through a monolayer of confining nanoparticles. Macromolecules 2020;53:8171–80. https://doi.org/10.1021/acs.macromol.0c01524.

[44] Shin K, Obukhov S, Chen JT, Huh J, Hwang Y, Mok S, Dobriyal P, Thiyagarajan P, Russell TP. Enhanced mobility of confined polymers. Nat Mater 2007;6:961–5. https://doi.org/10.1038/nmat2031.

[45] Yao Y, Alexandris S, Henrich F, Auernhammer G, Steinhart M, Butt HJ, Floudas G. Complex dynamics of capillary imbibition of poly(ethylene oxide) melts in nanoporous alumina. J Chem Phys 2017;146. https://doi.org/10.1063/1.4978298.

[46] Krutyeva M, Wischnewski A, Monkenbusch M, Willner L, Maiz J, Mijangos C, Arbe A, Colmenero J, Radulescu A, Holderer O, Ohl M, Richter D. Effect of nanoconfinement on polymer dynamics: surface layers and interphases. Phys Rev Lett 2013;110:1–5. https://doi.org/10.1103/PhysRevLett.110.108303.

[47] Milenov T, Avramova I. Deposition of graphene by sublimation of pyrolytic carbon. Opt Quant Electron 2015;47:851–63. https://doi.org/10.1007/s11082-014-0015-z.

[48] Hu XJ, Chen XH, Ye JS. The roles of hydrogen in the diamond/amorphous carbon phase transitions of oxygen ion implanted ultrananocrystalline diamond films at different annealing temperatures. AIP Adv 2012;2. https://doi.org/10.1063/1.4759087.

[49] Yuan Y, Jiao Y, Wang Y, Li S. Universality of jammed frictional packing. Phys Rev Res 2021;3. https://doi.org/10.1103/PhysRevResearch.3.033084.

[50] Stickel JJ, Powell RL. Fluid mechanics and rheology of dense suspensions. Annu Rev Fluid Mech 2005;37:129–49. https://doi.org/10.1146/annurev.fluid.36.050802.122132.

[51] Kaully T, Siegmann A, Shacham D. Rheology of highly filled natural CaCO3 composites. II. Effects of solid loading and particle size distribution on rotational rheometry. Polym Compos 2007;28:524–33. https://doi.org/10.1002/pc.20309.

[52] Fetters LJ, Lohse DJ, Milner ST, Graessley WW. Packing length influence in linear polymer melts on the entanglement, critical, and reptation molecular weights. Macromolecules 1999;32:6847–51. https://doi.org/10.1021/ma990620o.

[53] Doi M, Edward SF. The theory of polymer dynamics. Oxford: Clarendon Press; 1987. https://doi.org/10.11316/butsuri1946.42.4.370.

[54] Konijn BJ, Sanderink OBJ, Kruyt NP. Experimental study of the viscosity of suspensions : effect of solid fraction , particle size and suspending liquid Experimental study of the viscosity of suspensions : effect of solid fraction , particle size and suspending liquid. Powder Technol 2017;266:61–9. https://doi.org/10.1016/j.powtec.2014.05.044.

[55] Chen SB. Axisymmetric motion of multiple composite spheres: solid core with permeable shell, under creeping flow conditions. Phys Fluids 1998;10:1550–63. https://doi.org/10.1063/1.869676.

[56] Abade GC, Cichocki B, Ekiel-Jeewska ML, Nägele G, Wajnryb E. High-frequency viscosity of concentrated porous particles suspensions. J Chem Phys 2010;133. https://doi.org/10.1063/1.3474804.

[57] Granick S. Motions and relaxations of confined liquids. Science 1991;253:1374–9. https://doi.org/10.1126/science.253.5026.1374. 80-.

[58] Wang H, Hor JL, Zhang Y, Liu T, Lee D, Fakhraai Z. Dramatic increase in polymer glass transition temperature under extreme nanoconfinement in weakly interacting nanoparticle films. ACS Nano 2018;12:5580–7. https://doi.org/10.1021/acsnano.8b01341.

[59] Uemura T, Yanai N, Watanabe S, Tanaka H, Numaguchi R, Miyahara MT, Ohta Y, Nagaoka M, Kitagawa S. Unveiling thermal transitions of polymers in subnanometre pores. Nat Commun 2010;1. https://doi.org/10.1038/ncomms1091.

[60] Park JY, McKenna GB. Size and confinement effects on the glass transition behavior of polystyrene/o-terphenyl polymer solutions. Phys Rev B Condens Matter 2000;61:6667–76. https://doi.org/10.1103/PhysRevB.61.6667.

[61] Fatkullin N, Kimmich R, Fischer E, Mattea C, Beginn U, Kroutieva M. The confined-to-bulk dynamics transition of polymer melts in nanoscopic pores of solid matrices with varying pore diameter. New J Phys 2004;6. https://doi.org/10.1088/1367-2630/6/1/046.

[62] Huber P. Soft matter in hard confinement: phase transition thermodynamics, structure, texture, diffusion and flow in nanoporous media. J Phys Condens Matter 2015;27. https://doi.org/10.1088/0953-8984/27/10/103102.

[63] Isaacson SG, Lionti K, Volksen W, Magbitang TP, Matsuda Y, Dauskardt RH, Dubois G. Fundamental limits of material toughening in molecularly confined polymers. Nat Mater 2016;15:294–8. https://doi.org/10.1038/nmat4475.

[64] Maguire SM, Bilchak CR, Corsi JS, Welborn SS, Tsaggaris T, Ford J, Detsi E, Fakhraai Z, Composto RJ. Effect of nanoscale confinement on polymer-infiltrated scaffold metal composites. ACS Appl Mater Interfaces 2021;13:44893–903. https://doi.org/10.1021/acsami.1c12491.